Constraining cosmological ultra-large scale structure using numerical relativity

Jonathan Braden,[1,*] Matthew C. Johnson,[2,3,†] Hiranya V. Peiris,[1,‡] and Anthony Aguirre[4,§]

[1] *Department of Physics and Astronomy, University College London, London WC1E 6BT, U.K.*
[2] *Department of Physics and Astronomy, York University, Toronto, Ontario, M3J 1P3, Canada*
[3] *Perimeter Institute for Theoretical Physics, Waterloo, Ontario N2L 2Y5, Canada*
[4] *SCIPP and Department of Physics, University of California, Santa Cruz, CA, 95064, USA*

(Dated: May 4, 2016)

Cosmic inflation, a period of accelerated expansion in the early universe, can give rise to large amplitude ultra-large scale inhomogeneities on distance scales comparable to or larger than the observable universe. The cosmic microwave background (CMB) anisotropy on the largest angular scales is sensitive to such inhomogeneities and can be used to constrain the presence of ultra-large scale structure (ULSS). We numerically evolve nonlinear inhomogeneities present at the beginning of inflation in full General Relativity to assess the CMB quadrupole constraint on the amplitude of the initial fluctuations and the size of the observable universe relative to a length scale characterizing the ULSS. To obtain a statistically meaningful ensemble of simulations, we adopt a toy model in which inhomogeneities are injected along a preferred direction. We compute the likelihood function for the CMB quadrupole including both ULSS and the standard quantum fluctuations produced during inflation. We compute the posterior given the observed CMB quadrupole, finding that when including gravitational nonlinearities, ULSS curvature perturbations of order unity are allowed by the data, even on length scales not too much larger than the size of the observable universe. Our results illustrate the utility and importance of numerical relativity for constraining early universe cosmology.

Cosmic inflation, a postulated era of accelerated expansion in the early universe, has become an integral part of modern cosmology; but while inflation provides a dynamical mechanism to produce the initial conditions for the standard hot Big Bang cosmology, the initial conditions for inflation itself are far more uncertain. Cosmological measurements are bounded by the cosmological horizon, placing fundamental limits on our direct knowledge of the universe on arbitrarily large scales. However, many inflationary models — for example those including "eternal" inflation [1, 2] or starting from inhomogeneous initial conditions — lead to a rich and complicated structure on ultra-large scales compared to our own local Hubble volume. It is thus of great interest to look for ways to probe this structure using "local" measurements of the observable universe.

In this *Letter* we study the effects of nonlinear inhomogeneities present at the beginning of single-scalar field inflation on the quadrupole of the cosmic microwave background (CMB) radiation observed today, a phenomenon known as the Grischuk-Zel'dovich (GZ) effect [3]. Because pre-inflationary physics primarily affects the largest scales of the observable universe, the CMB quadrupole is the most important observable in this context. Previous studies of the GZ effect (e.g., [4, 5]) neglect the effect of gravitational nonlinearities, basing their inferences on Gaussian statistics. However, the large gravitational nonlinearities studied in this scenario could plausibly lead to significant non-Gaussianity, which in turn affect our inferences about ultra-large scale structure (ULSS).

This motivates the fully General Relativistic numerical treatment that we undertake in this work. For computational efficiency, we study a toy model that assumes primordial inhomogeneities are only present along a preferred spatial direction, allowing us to perform simulations in one spatial dimension. The model is specified by the choice of inflationary potential, the spectral shape and amplitude of primordial inhomogeneities in the scalar field, and the infrared and ultraviolet cutoff on scales contributing to the initial inhomogeneities. Using highly accurate numerical techniques, we are able evolve realizations of these pre-inflationary fluctuations well into the post-inflationary regime using mere seconds of computing time, while maintaining convergence to the level of machine precision. This numerical efficiency allows us to sample many realizations of the initial conditions to build up a statistical description of observables in our model.

For three qualitatively different choices of the inflationary potential, we vary the initial fluctuation amplitude and build up a set of probability distributions over the locally observed $\ell = 2$ CMB multipole, a_{20}, at different spatial positions. We find that independent of the inflationary model, and under a variety of physically plausible weighting schemes for spatial positions, nonlinear gravitational effects yield a highly non-Gaussian distribution for a_{20}. We then fold into our calculation the standard smaller-wavelength vacuum fluctuations generated by inflation, to obtain the probability distribution of power in the observed CMB quadrupole. The relative contribution of the ULSS and vacuum fluctuations is controlled by a variable that maps primordial length scales to present-day length scales.

We compute the full posterior over the initial fluctuation amplitude and mapping parameter, comparing with

what would have been obtained if gravitational nonlinearities had not been taken into account. We conclude it is essential to accurately model gravitational nonlinearities to make accurate inferences about ULSS from measurements of the CMB quadrupole. We expect similar qualitative conclusions to hold in the case where no symmetry assumptions are made, and we comment on the broader implications of our result to this more realistic scenario. More generally, our results motivate a systematic study of the influence of strong gravity in the early universe on cosmological observables.

Models and numerical methods: We consider planar-symmetric inflationary initial conditions in the α attractor models of inflation [6], with Lagrangian density

$$\mathcal{L} = -\frac{1}{2}\partial_\mu\phi\partial^\mu\phi - V_0\left(1 - e^{-\sqrt{\frac{2}{3\alpha}}\frac{\phi}{M_P}}\right)^2 . \quad (1)$$

Large- and small-field models are characterized by the field excursion relative to $M_{\rm P}$ during the final 60 e-folds of inflation and by their prediction for the primordial tensor-to-scalar ratio through the Lyth bound [7]. This class of models conveniently interpolates between large-field inflation at $\alpha \gg 1$ and small-field inflation at $\alpha \ll 1$. Current limits favor intermediate and small-field models [8]. We analyzed three representative models: $\alpha \to \infty$ (equivalent to a quadratic inflationary potential [9]), $\alpha = 2/3$ (similar to Starobinsky's R^2 inflation [10], where $\alpha = 1$), and $\alpha = 2/300$ (where inflation occurs on a flat plateau). In all three cases we found qualitatively similar behaviour. To illustrate the basic phenomenology, we present results for the numerically challenging case of $\alpha = 2/300$ below.

We assume our spacetime possesses two spatial translation isometries and choose a synchronous gauge with metric

$$ds^2 = -d\tau^2 + a_\parallel^2(x,\tau)dx^2 + a_\perp^2(x,\tau)\left(dy^2 + dz^2\right) . \quad (2)$$

The full set of evolution and constraint equations resulting from Einstein's equations are included in the supplemental material. We introduce the field momenta $\Pi_\phi \equiv a_\parallel\dot{\phi}$ (with $\dot{\phi} \equiv \partial_\tau\phi$) and the extrinsic curvatures $K^x{}_x$ and $K^y{}_y$ to obtain first order equations of motion. We also define $H_{\rm I}^2 \equiv V(\bar{\phi}(\tau=0))/3M_{\rm P}^2$, where $\bar{\phi}(\tau=0)$ is the average value of the field on the initial conditions surface $\tau = 0$. Below, we measure fields in terms of $M_{\rm P}$.

We choose the coordinates x, y, and z to measure proper distance on the initial spatial slice, corresponding to $a_\parallel(\tau=0,x) = a_\perp(\tau=0,x) = 1$. The initial conditions for each simulation can then be specified entirely in terms of ϕ and Π_ϕ. Once these are given, we solve the momentum constraint for $K^y{}_y$, and finally substitute into the Hamiltonian constraint to obtain an algebraic equation for $K^x{}_x$. See the supplemental material for the full form of the constraint equations.

We take the scalar field on the initial surface to be $\phi(\tau=0,x) = \bar{\phi} + \delta\hat{\phi}(x)$ and $\Pi_\phi(x) = \bar{\Pi}_\phi = 0$. The mean field $\bar{\phi}$ is set to obtain 60 e-folds of inflation in the homogeneous slow-roll approximation. The normalization V_0 is chosen to match the amplitude of scalar power measured by the *Planck* satellite [13]. The fluctuations $\delta\hat{\phi}(x)$ are drawn from a one-dimensional Gaussian random field with a band-pass filtered white noise spectrum

$$\delta\hat{\phi}(x_i) = A_\phi \sum_{n=n_{\rm IR}}^{n_{\rm UV}} e^{ik_n x_i}\tilde{G}_n \qquad i = 1,\ldots,N\,, \quad (3)$$

where $k_n \equiv 2\pi\frac{n}{L}$, $x_i = idx$, $\tilde{G}_n$ are realizations of complex Gaussian random deviates with $\langle|\tilde{G}|^2\rangle = 2$, and A_ϕ is a free parameter. We choose $n_{\rm IR} = 1$, $n_{\rm UV} = \sqrt{3}H_{\rm I}L$ and a box size $H_{\rm I}L = 256/\sqrt{3}$, corresponding to modes spanning the range $\frac{2\pi}{256}\sqrt{3} < H_{\rm I}^{-1}k < 2\pi\sqrt{3}$ in wavenumber.

The evolution equations are solved numerically using a 10th order Gauss-Legendre time integrator [14, 15] and a Fourier collocation-based spatial discretization [16]. As expected, the code displays exponential convergence with spatial resolution and tenth order convergence with temporal resolution. We evolve from the initial pre-inflationary hypersurface until several e-folds after the onset of post-inflation scalar field oscillations everywhere in the simulation volume. During this evolution, the relevant dynamical time scale varies greatly, requiring adaptive time-stepping. We are able evolve a grid of 4096 points in approximately 10 seconds on a single core. All dynamical fields are resolved to machine precision, with a similar accuracy in preserving constraints. For each of the three potentials, this numerical efficiency allows us to explore a range of amplitudes A_ϕ spanning between four and six orders of magnitude (depending on the model), running 100 realizations of the Gaussian initial conditions at each amplitude.

Extracting cosmological observables: The CMB quadrupole as viewed from each location in the simulation is determined by the comoving curvature perturbation $\zeta_{\rm end}$ at the end of inflation, along with the cosmological redshift to the end-of-inflation hypersurface. There are a variety of methods to find $\zeta_{\rm end}$ [17–19]. Here we follow the $\delta\mathcal{N}$ formalism [20, 21] and compute

$$\zeta(H) = \frac{1}{6}\ln\det\gamma_{ij}\big|^{-\frac{1}{3}K_i{}^i=H}_{a_\parallel=a_\perp=1} = \ln(a) \quad (4)$$

where $\gamma_{ij} = {\rm diag}(a_\parallel^2, a_\perp^2, a_\perp^2)$ is the spatial three-metric on fixed τ slices and $a \equiv \left(a_\parallel a_\perp^2\right)^{1/3}$. ζ is defined on hypersurfaces of constant $H \equiv -\frac{1}{3}K_i^i$ as measured by comoving observers. The proper distance along these hypersurfaces in terms of our original x coordinate is

$$dx^2_{H={\rm const}} = a_\parallel^2\left(1 - \frac{H'^2}{a_\parallel^2\dot{H}^2}\right)dx^2\,, \quad (5)$$

where $H' \equiv \partial_x H$. The hypersurface on which inflation ends is defined by the first occurrence of $\epsilon_H \equiv$

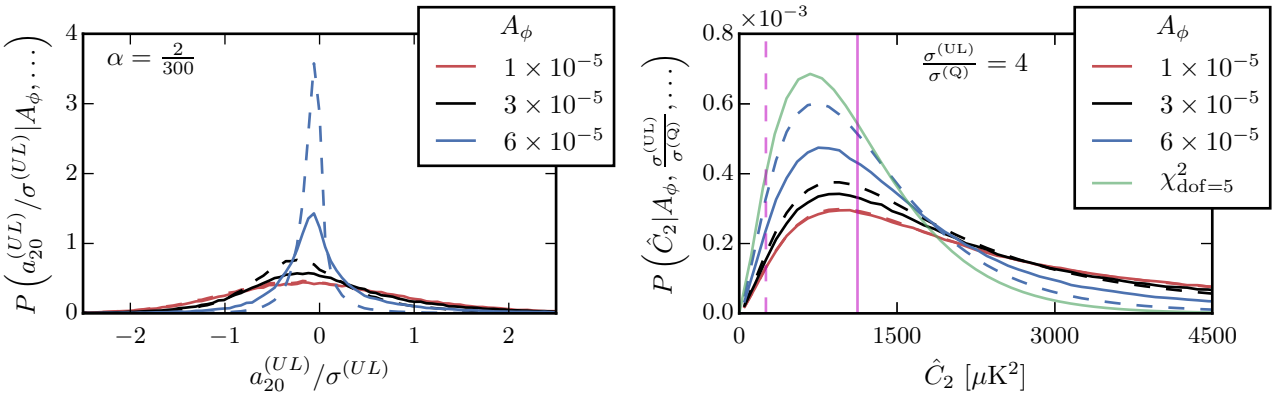

FIG. 1: *Left*: PDF for the $\ell = 2$ CMB multipole $a_{20}^{(\rm UL)}$ generated by ULSS, scaled to $\sigma^{(\rm UL)} \equiv \sqrt{\langle a_{20}^{(\rm UL)\,2}\rangle}$. As the amplitude of the initial fluctuations is varied, the distribution becomes increasingly non-Gaussian and peaked. *Right*: Sampling distribution of the estimator $\hat{C}_2$ in Eq. 7. The solid vertical magenta line is the mean value predicted by the best-fit ΛCDM model from the *Planck* data, and the dashed vertical magenta line is the observed value. In both panels, solid lines are the distributions for comoving volume weighting and dashed lines are for physical volume weighting.

$-d\ln H/d\ln a = 1$ at each spatial position. After a short transient, ϵ_H is a function of H alone, in agreement with the separate universe assumption [22]. Therefore, $\zeta_{\rm end}$ corresponds to the particular choice $\zeta(H_{\rm end})$. Note that ζ quantifies the overall expansion of a local packet of geodesics, so variations in the value of ζ as a function of position encodes the comoving curvature perturbation. After a short transient, spatial variations in ζ freeze in.

The terms in a Taylor series expansion of $\zeta_{\rm end}$ around each point x_p^n along the end-of-inflation hypersurface are related to the properties of a set of locally-defined nearly homogeneous patches, which can in turn be related to the observed CMB at each position. The constant term in the expansion $\zeta_{\rm end}(x_p^n)$ is the natural logarithm of the local scale factor (recall that our definition of ζ contains the mean expansion), which is not directly observable. The first derivative term also does not lead to any observable signatures, since pure gradients in the gravitational potential are pure gauge [5, 23]. The leading observable is therefore the quadratic term in the expansion, which maps onto a CMB quadrupole through the Sachs-Wolfe and Integrated Sachs-Wolfe effect. For the situation we focus on, this truncated expansion encapsulates all observable effects of ULSS. (There are other situations, for example cosmic bubble collisions in eternal inflation [17, 19, 24], where discontinuities lead to a more complicated mapping between the curvature perturbation and the observable CMB signature.)

Rotating the coordinate system appropriately, only the $m = 0$ mode of the $\ell = 2$ CMB temperature anisotropy is non-zero, and we can write

$$a_{20}^{(UL)} = F(L_{\rm obs}H_{\rm I})^2\partial_{x_p}^2\zeta \simeq F(L_{\rm obs}H_{\rm I})^2\frac{1}{a_\parallel}\partial_x\left[\frac{\partial_x\zeta}{a_\parallel}\right]. \quad (6)$$

Here F is a constant factor encoding constants of order unity, a correction from the Integrated Sachs-Wolfe effect, and a conversion from proper distance along the end-of-inflation hypersurface to comoving distance at last scattering. $L_{\rm obs}$ is the comoving radius of the surface of last scattering, and $H_{\rm I}$ is the average Hubble parameter at the beginning inflation. In the final approximation, we have assumed $(H'/a_\parallel\dot{H})^2 \sim k_{\rm max}^2/a_\parallel^2H^2\epsilon^2 \ll 1$, with $k_{\rm max}$ the largest excited wavenumber in the Fourier transform of H on uniform τ slices. This is valid on the inflation-ending hypersurface when the local Hubble expansion rate only varies on scales much larger than the local Hubble horizon.

The combination $L_{\rm obs}H_{\rm I}$ is a free parameter, and encodes the mapping of primordial length scales to length scales at last scattering, which depends on the details of reheating, number of e-folds of inflation, etc. We have chosen our conventions such that in the homogeneous limit, $L_{\rm obs}H_{\rm I} = 1$ is the necessary condition for solving the horizon problem, which translates into the observable universe being descended from a single causally-connected domain at the beginning of inflation of physical size $H_{\rm I}^{-1}$. Since the perturbations freeze out, this normalization ensures that our results are independent of the particular Hubble slice we use for ζ extraction. In the small-amplitude limit, $H_{\rm I}^{-1}$ translates into the local comoving scale of inhomogeneity. For the case of strong inhomogeneity, this identification is lost due to the strong spatial dependence of the gauge transformation to comoving coordinates and the generation of smaller-scale fluctuations through mode-mode coupling.

Simulation Results: Parametrizing the end-of-inflation hypersurface by the coordinate x, we extract the locally-observed CMB quadrupole Eq. 6 at each position in each simulation. Additionally, the distribution over $a_{20}^{(\rm UL)}$ depends on the probability (or weight) that we assign to an imaginary observer at each grid point. We con-

sider two weighting schemes. In comoving volume weighting, we equally weight observations at each grid point on the end of inflation surface. Because each coordinate position x labels a geodesic through the space-time, our simulation coordinates naturally preserve comoving volume (see also Ref. [25]). In physical volume weighting, we weight observations at each position x by the total growth in physical volume during inflation, $e^{3\zeta_{\rm end}(x)}$. Empirical PDFs are created by binning the $a_{20}^{(\rm UL)}$ samples by their assigned weights to produce a normalized histogram. We confirmed that smoothing the empirical cumulative distribution function (CDF) and differentiating it produces the same distributions.

Several representative PDFs for the small-field model of inflation ($\alpha = 2/300$) are shown in the left panel of Fig. 1. The PDFs for the comoving volume weighting scheme are denoted by solid lines and those for physical volume weighting by dashed lines. Note that the PDFs in Fig. 1 are normalized to their variance; unnormalized distributions would have a variance that increases with A_ϕ, spanning $8\times10^{-2} < \sigma^{(\rm UL)} \lesssim 10^{13}$ over the range $10^{-6} \leq A_\phi \leq 10^{-3}$.

For small amplitudes A_ϕ the distribution is Gaussian, as expected from the linear evolution of the Gaussian initial conditions for $\delta\hat{\phi}$. In this regime, there is no significant difference between the weighting schemes. As A_ϕ is increased, gravitational nonlinearities become more important, with variations in ζ becoming order unity for $A_\phi \gtrsim 4\times10^{-5}$ in the small-field model. In this same limit, the PDFs gain a more pronounced non-Gaussian shape, primarily in the form of an increasing kurtosis. The PDFs also develop a skew towards negative values for $a_{20}^{(\rm UL)}$, indicating a bias towards peaks in ζ over troughs, as well as a non-zero mean. For very large amplitudes, the distribution becomes very sharply peaked about $a_{20}^{(\rm UL)} = 0$.

In the highly nonlinear regime, for both weighting schemes, most of the volume on the reheating surface is descended from regions that were further up the potential, and therefore have undergone a larger amount of inflation than in the homogeneous limit (see also [26, 27]). This unequal weighting explains the negative skew of the PDF for $a_{20}^{(\rm UL)}$, as regions that inflate more are likely to be associated with peaks rather than troughs. It also explains the limiting form of the PDF, since for most of the volume on the reheating surface, inhomogeneities would have been blown up to extremely large scales.

Overall, the two weighting schemes produce qualitatively similar results, with the amplitude A_ϕ at which non-Gaussianities become apparent being lower for the volume weighting scheme. This is also the main difference between the inflationary potentials, where the threshold A_ϕ at which ζ becomes order one is larger in the intermediate ($\alpha = 2/3$) and large-field ($\alpha \to \infty$) models. This is simply a reflection of the increased sensitivity to the initial conditions in small-field models as compared to large-field models [28]: as ζ gets large, primordial inhomogeneities can ruin inflation in some regions (e.g., [29]).

To facilitate the comparison of the predictions of our toy model with the observed CMB angular power spectrum, we combine the effects on a_{20} of ULSS and the standard inflationary quantum fluctuations that give rise to structure on sub-horizon scales. In our toy model ULSS is present in only one spatial direction, and contribute only to a_{20}. A more realistic, but computationally infeasible, scenario would have contributions to all 5 of the a_{2m} in addition to a contribution to the locally-observed spatial curvature.

The observed CMB quadrupole is constructed from the sample variance $\hat{C}_2$. In our toy model, a particular realization would yield

$$\hat{C}_2 = \frac{1}{5}\left[\left(a_{20}^{(\rm UL)} + a_{20}^{(\rm Q)}\right)^2 + \sum_{m=-2,\ m\neq0}^{2}\left(a_{2m}^{(\rm Q)}\right)^2\right], \quad (7)$$

where $a_{20}^{(\rm UL)}$ is drawn from distributions analogous to those shown in the left panel of Fig. 1 and $a_{20}^{(\rm Q)}$ is drawn from a Gaussian distribution of variance $\sigma^{(\rm Q)} = 1124.1\,\mu{\rm K}^2$, in agreement with the current best-fit ΛCDM parameters from the *Planck* satellite [13]. In the right panel of Fig. 1, we show the predicted probability distribution over $\hat{C}_2$, generated by drawing realizations $\hat{C}_2$ (Eq. 7), fixing the variance of $a_{20}^{(\rm UL)}$ to be 4 times larger than that of $a_{20}^{(\rm Q)}$. For comparison, we show the PDF over $\hat{C}_2$ in the absence of ULSS (a χ^2 distribution with 5 degrees of freedom). As shown in Fig. 1, there is no significant qualitative difference between the two weighting schemes.

Surprisingly, Fig. 1 shows that *for fixed relative RMS*, larger initial amplitudes A_ϕ become increasingly indistinguishable from the case of no ULSS contribution, where C_2 is drawn from a $\chi^2_{\rm dof=5}$ distribution. At the level of Eq. 7, this is because draws for $a_{20}^{(\rm UL)}$ are nearly all in the vicinity of the peak of the PDF, which is far smaller than the variance of the distribution, so that $a_{20}^{(\rm UL)} \ll a_{20}^{(\rm Q)}$ in most realizations.

Observational constraints: The CMB quadrupole obtained using the `Commander` approach on *Planck* 2015 data is $\hat{C}_2^{\rm obs} = 253.6\,\mu{\rm K}^2$ [33]. The central value lies near the lower 95% confidence level bound of the best-fit ΛCDM model in the absence of ULSS. This arguably anomalously low value for the CMB quadrupole has received note since the first full-sky measurements of the CMB angular power spectrum by the COBE satellite [30]. Our model does not address this issue.

Given $\hat{C}_2^{\rm obs}$, we derive constraints on the presence of ULSS by computing the posterior $P(\log_{10} A_\phi, \log_{10} L_{\rm obs}H_{\rm I}|\hat{C}_2^{\rm obs})$, shown in Fig. 2 for the model with $\alpha = 2/300$ and comoving volume

weighting. In computing the posterior, we assume uniform priors on $\log_{10} A_\phi$ and $\log_{10} H_{\rm I} L_{\rm obs}$ in the ranges $-6 \leq \log_{10} A_\phi \leq -3$ and $-5 \leq \log_{10} L_{\rm obs} H_{\rm I} \leq 0$. The upper bound on $\log_{10} A_\phi$ corresponds to the point where our numerics break down (well into the nonlinear regime), and the upper bound on $\log_{10} H_{\rm I} L_{\rm obs}$ is the value required to solve the horizon problem. Note that the model without ULSS is at $A_\phi = L_{\rm obs} H_{\rm I} = 0$, which maximizes the posterior.

In Fig. 2, we also show contours (dashed lines) for the posterior generated under the assumption that the ultra-large scale modes are drawn from a purely Gaussian distribution of equal variance to the numerically derived non-Gaussian PDFs. This is equivalent to comparing to the case in which gravitational nonlinearities are neglected. As expected, for small A_ϕ where the PDFs are approximately Gaussian, there is good agreement. However, as A_ϕ is increased, and the PDFs become increasingly non-Gaussian, the posterior has far more weight at larger $L_{\rm obs} H_{\rm I}$ than is obtained with Gaussian PDFs. Therefore, in the nonlinear regime, it becomes relatively more *difficult* to constrain ULSS.

Comparing the posterior generated for the different models of inflation and different weighting schemes, we obtain functions qualitatively similar to that shown in Fig. 2. In physical volume weighting, the deviations from the Gaussian model arise at relatively smaller values of A_ϕ and larger values of $H_{\rm I} L_{\rm obs}$. This can be traced back to the onset of non-Gaussianities in $a_{20}^{\rm (UL)}$ at smaller values of A_ϕ for physical volume weighting (see Fig. 1). For large-field and intermediate models of inflation, the onset of deviations from the Gaussian model arise at larger values of A_ϕ and smaller values of $H_{\rm I} L_{\rm obs}$ than for the small-field model. Therefore, while the precise constraints from the posterior depend on the inflationary potential and weighting scheme, the result Fig. 2 is qualitatively robust.

Conclusions: We have studied a toy model in which ultra-large scale structure (ULSS) is generated from the nonlinear evolution of large amplitude inhomogeneities in the initial conditions for inflation in a single spatial direction. In this setting, we have found a non-Gaussian probability distribution over the imprint of ULSS on the CMB quadrupole. We find that in cases where inflation is not completely disrupted, large amplitude pre-inflationary ULSS is allowed by current data over a wide range in mapping scales $H_{\rm I} L_{\rm obs}$.

Qualitatively, we expect the same to be true in a more realistic scenario where primordial inhomogeneities have no assumed symmetries. In a crude approximation, we might guess that the contribution to a_{2m} from ULSS for each m is drawn from the non-Gaussian distributions of our toy model. The contribution from ULSS to the spatial curvature would be drawn from an analogously non-Gaussian distribution, making it less likely to observe spatial curvature than in previous computations that neglect gravitational nonlinearities [31, 32].

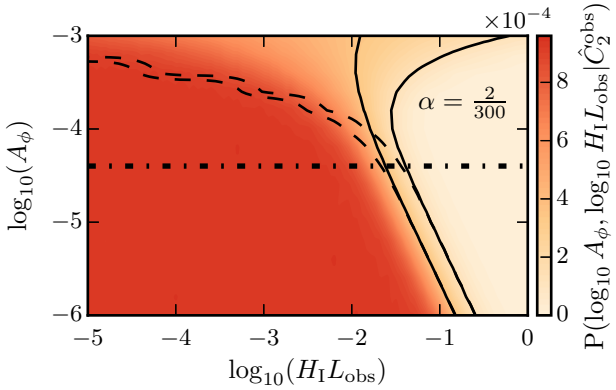

FIG. 2: The posterior probability distribution for our model parameters $\log_{10}(A_\phi)$ and $\log_{10}(H_{\rm I} L_{\rm obs})$ with uniform priors in the range $(-6, -3)$ and $(-5, 0)$ respectively. The solid lines are the contours at which the posterior drops to e^{-1} and e^{-2} of its maximal value. The dashed curves are the same contours if we model $a_{20}^{\rm (UL)}$ in Eq. 7 as a Gaussian random variable with the same RMS as the distributions in Fig. 1. The dot-dashed line indicates the initial amplitude A_ϕ at which $\sigma_\zeta = 1$.

More generally, this work illustrates the novel possibility of applying the tools of numerical General Relativity to formulate precise tests of early universe physics. As we reach the limit on accessible information about the primordial universe, precise tools for making theoretical predictions are essential for getting the most information possible from the limited observations that we are able to make.

JB and HVP are supported by the European Research Council under the European Community's Seventh Framework Programme (FP7/2007-2013) / ERC grant agreement no 306478-CosmicDawn. MCJ is supported by the National Science and Engineering Research Council through a Discovery grant. Research at Perimeter Institute is supported by the Government of Canada through Industry Canada and by the Province of Ontario through the Ministry of Research and Innovation. AA was supported in part by time release grant FQXi-PO-1501 from the Foundational Questions Institute (FQXi), of which he is Associate Director. This work was supported in part by National Science Foundation Grant No. PHYS-1066293 and the hospitality of the Aspen Center for Physics. We also thank the Department of Physics at the University of Auckland for hospitality during the completion of this work. We thank R. Easther, D. Mortlock, and E. Lim for useful conversations.

Supplemental Material

In this supplemental material, we present the full evolution and constraint equations used above. We focus on the evolution of a canonically normalized scalar field minimally coupled to gravity with action

$$S = \int d^4x\sqrt{-g}\left[\frac{1}{2M_p^2}R + \mathcal{L}(\partial_\mu\phi,\phi)\right], \tag{8}$$

where R is the four dimensional Ricci scalar and $\mathcal{L}(\partial_\mu\phi,\phi)$ is the Lagrangian density for the inflaton Eq. 1. Varying the action, and assuming a metric of the form Eq. 2 with two free functions $a_\parallel(x,\tau)$ and $a_\perp(x,\tau)$, one obtains a coupled set of partial differential equations with mixed first and second time derivatives. By introducing the components of the extrinsic curvature tensor $K^x{}_x(x,\tau)$ and $K^y{}_y(x,\tau)$, it is possible to isolate a first-order in time system of evolution equations for the gravitational sector and the matter sector:

$$\dot{a_\parallel} = -a_\parallel K^x{}_x, \tag{9a}$$
$$\dot{a_\perp} = -a_\perp K^y{}_y, \tag{9b}$$
$$\dot{K^x{}_x} = \frac{a_\perp'^2}{a_\perp^2 a_\parallel^2} + {K^x{}_x}^2 - {K^y{}_y}^2 + \frac{\left(\Pi_\phi^2 - \phi'^2\right)}{2a_\parallel^2 M_{\rm P}^2}, \tag{9c}$$
$$\dot{K^y{}_y} = -\frac{a_\perp'^2}{2a_\perp^2 a_\parallel^2} + \frac{3}{2}{K^y{}_y}^2 - \frac{V(\phi)}{2M_{\rm P}^2} + \frac{\left(\Pi_\phi^2 + \phi'^2\right)}{4a_\parallel^2 M_{\rm P}^2}, \tag{9d}$$
$$\dot{\Pi}_\phi = 2K^y{}_y\Pi_\phi + \frac{1}{a_\parallel}\phi'' + \left(\frac{2a_\perp'}{a_\parallel a_\perp} - \frac{a_\parallel'}{a_\perp^2}\right)\phi' - a_\perp\partial_\phi V(\phi), \tag{9e}$$
$$\dot{\phi} = \frac{\Pi_\phi}{a_\parallel}. \tag{9f}$$

There are also two constraint equations, the Hamiltonian ($\mathcal{H}$) and momentum ($\mathcal{P}$) constraints, given by:

$$\mathcal{H} = \frac{2a_\perp a_\parallel' a_\perp' - a_\parallel a_\perp'^2 - 2a_\parallel a_\perp a_\perp''}{a_\parallel^3 a_\perp^2} + 2K^x{}_x K^y{}_y + {K^y{}_y}^2 - M_{\rm P}^{-2}\left(\frac{\phi'^2 + \Pi_\phi^2}{2a_\parallel^2} + V\right), \tag{10a}$$
$$\mathcal{P} = {K^y{}_y}' - \frac{a_\perp'}{a_\perp}\left(K^x{}_x - K^y{}_y\right) - \frac{\phi'\Pi_\phi}{2a_\parallel M_{\rm P}^2}. \tag{10b}$$

Both the Hamiltonian and momentum constraints should be zero for exact solutions to Einstein's equations. Numerically, we require that they remain as small as possible.

* Electronic address: j.braden@ucl.ac.uk
† Electronic address: mjohnson@perimeterinstitute.ca
‡ Electronic address: h.peiris@ucl.ac.uk
§ Electronic address: aguirre@scipp.ucsc.edu

[1] A. Aguirre, in *Beyond the Big Bang* (Springer, 2008).
[2] A. H. Guth, J.Phys. **A40**, 6811 (2007), hep-th/0702178.
[3] L. P. Grischuk and Y. B. Zel'Dovich, Astron. Zh. **55**, 209 (1978).
[4] P. G. Castro, M. Douspis, and P. G. Ferreira, Phys. Rev. **D68**, 127301 (2003), astro-ph/0309320.
[5] M. S. Turner, Phys. Rev. **D44**, 3737 (1991).
[6] R. Kallosh, A. Linde, and D. Roest, JHEP **11**, 198 (2013), 1311.0472.
[7] D. H. Lyth, Phys. Rev. Lett. **78**, 1861 (1997), hep-ph/9606387.
[8] P. Ade et al. (BICEP2, Planck), Phys. Rev. Lett. **114**, 101301 (2015), 1502.00612.
[9] A. D. Linde, Phys. Lett. **B129**, 177 (1983).
[10] A. A. Starobinsky, Phys. Lett. **B91**, 99 (1980).
[11] D. S. Salopek, J. R. Bond, and J. M. Bardeen, Phys. Rev. **D40**, 1753 (1989).
[12] F. L. Bezrukov and M. Shaposhnikov, Phys. Lett. **B659**, 703 (2008), 0710.3755.
[13] P. A. R. Ade et al. (Planck) (2015), 1502.01589.
[14] J. Braden, J. R. Bond, and L. Mersini-Houghton, JCAP **1503**, 007 (2015), 1412.5591.
[15] J. Butcher, Math. Comp. **18**, 50 (1964).
[16] J. P. Boyd, *Chebyshev and Fourier spectral methods* (Dover Publ. cop., 2001).
[17] C. L. Wainwright, M. C. Johnson, H. V. Peiris, A. Aguirre, L. Lehner, et al., JCAP **1403**, 030 (2014), 1312.1357.
[18] B. Xue, D. Garfinkle, F. Pretorius, and P. J. Steinhardt, Phys.Rev. **D88**, 083509 (2013), 1308.3044.
[19] M. C. Johnson, C. L. Wainwright, A. Aguirre, and H. V. Peiris (2015), 1508.03641.
[20] D. S. Salopek and J. R. Bond, Phys. Rev. **D42**, 3936 (1990).
[21] M. Sasaki and E. D. Stewart, Prog.Theor.Phys. **95**, 71 (1996), astro-ph/9507001.
[22] A. A. Starobinsky, *Field Theory, Quantum Gravity and Strings* (Springer Berlin Heidelberg, 1986), chap. Stochastic de sitter (inflationary) stage in the early universe, pp. 107–126.
[23] A. L. Erickcek, S. M. Carroll, and M. Kamionkowski, Phys.Rev. **D78**, 083012 (2008), 0808.1570.
[24] C. L. Wainwright, M. C. Johnson, A. Aguirre, and H. V. Peiris, JCAP **1410**, 024 (2014), 1407.2950.
[25] A. Aguirre, S. Gratton, and M. C. Johnson, Phys. Rev. **D75**, 123501 (2007), hep-th/0611221.
[26] J. Garriga, D. Schwartz-Perlov, A. Vilenkin, and S. Winitzki, JCAP **0601**, 017 (2006), hep-th/0509184.
[27] A. D. Linde, JCAP **0701**, 022 (2007), hep-th/0611043.
[28] R. Brustein and P. J. Steinhardt, Phys. Lett. **B302**, 196 (1993), hep-th/9212049.
[29] W. E. East, M. Kleban, A. Linde, and L. Senatore (2015), 1511.05143.
[30] G. Hinshaw, A. J. Banday, C. L. Bennett, K. M. Gorski, A. Kogut, G. F. Smoot, and E. L. Wright, ApjL **464**, L17 (1996), astro-ph/9601058.
[31] M. Vardanyan, R. Trotta, and J. Silk, Mon. Not. Roy. Astron. Soc. **397**, 431 (2009), 0901.3354.
[32] M. Kleban and M. Schillo, JCAP **1206**, 029 (2012), 1202.5037.
[33] Available from the Planck Legacy Archive at `http://`

pla.esac.esa.int/pla/#cosmology